

Theoretical Study of a Two-Degree-of-Freedom Piezoelectric Energy Harvester under Concurrent Aeroelastic and Base Excitation

Guobiao Hu^{1,2}, Chunbo Lan³, Junrui Liang¹,
Lihua Tang² and Liya Zhao⁴

Abstract

This paper presents a study of a two-degree-of-freedom (2DOF) piezoelectric energy harvester (PEH) under concurrent aeroelastic and base excitation. The governing equations of the theoretical model under the combined excitation are developed and solved analytically using the harmonic balance method. Based on the electro-mechanical analogies, an equivalent circuit model is established. The energy harvesting performance of the 2DOF PEH under different wind speeds but the same base excitation is investigated. Voltage amplitudes of various response components with different frequencies are predicted by the analytical method and verified by the circuit simulation. The root-mean-square (RMS) voltage is used to measure the actual performance of the 2DOF PEH. Around the resonance state, the 2DOF PEH has been found to produce a larger voltage output than the conventional SDOF PEH. Moreover, several interesting phenomena, such as the quasi-periodic oscillation and the peak-to-valley transition, have been observed in the circuit simulation and explained by the analytical solution. The developed methodology in this paper can be easily adapted to analyze other similar types of multiple-degree-of-freedom (MDOF) PEHs under concurrent aeroelastic and base excitation.

Keywords

Concurrent energy harvesting, two-degree-of-freedom, galloping, piezoelectric

I. Introduction

Harvesting renewable energy from surrounding sources to realize perpetual environmentally powered wireless sensor networks has attracted numerous research interests in the past two decades (Fang et al., 2020; Li et al., 2021; Liang and Liao, 2012; Liu et al., 2019b; Paulo and Gaspar, 2010; Priya and Inman, 2009; Roundy et al., 2003; Wu et al., 2019; Zeadally et al., 2020). The wind is one of the most ubiquitous energy sources in nature. It has been extensively exploited for large-scale power generation over the world since the end of the last century (Staggs et al., 2017). Though the industrial wind energy technology has been maturely developed, harnessing wind energy to power micro-electro-mechanical systems (MEMS) is a relatively emerging research direction (Wang et al., 2020a). Unlike the rotary turbine design of a windmill, a wind energy harvester needs to be designed in a compact form to integrate with miniaturized MEMS. The motion of a vibrating system often requires less space than a rotating system. Therefore, researchers explored various

flow-induced vibration mechanisms to convert wind energy into vibrations and then realize electromechanical energy transduction based on the design philosophy of classic vibration energy harvesters (VEHs).

Common flow-induced vibration phenomena include galloping (Ali et al., 2013; Barrero-Gil et al., 2010;

¹School of Information Science and Technology, ShanghaiTech University, Shanghai, China

²Department of Mechanical Engineering, University of Auckland, Auckland, New Zealand

³College of Aerospace Engineering, Nanjing University of Aeronautics and Astronautics, Nanjing, Jiangsu, China

⁴School of Mechanical and Mechatronic Engineering, University of Technology Sydney, Sydney, NSW, Australia

Corresponding authors:

Junrui Liang, School of Information Science and Technology, ShanghaiTech University, 393 Middle Huaxia Road, Shanghai 201210, China.
Email: liangjr@shanghaitech.edu.cn

Lihua Tang, Department of Mechanical Engineering, University of Auckland, 20 Symonds Street, Auckland 1010, New Zealand.
Email: l.tang@auckland.ac.nz

Journal of Intelligent Material Systems and Structures

2022, Vol. 33(15) 2000–2016

© The Author(s) 2022

Article reuse guidelines:

sagepub.com/journals-permissions

DOI: 10.1177/1045389X211072520

journals.sagepub.com/home/jim



Sirohi and Mahadik, 2012), vortex-induced vibration (VIV) (Wang et al., 2019a; Zhang et al., 2020), wake galloping (Liu et al., 2020; Yan et al., 2020), and flutter (Eugeni et al., 2020). The galloping phenomenon could result in the self-excited vibration of the system around its natural frequency. The oscillation amplitude is expectably large as the system enters the resonance state. The galloping-induced aerodynamic force can be deemed a negative damping force from the mathematical point of view. After the wind speed exceeds the critical value, which is termed as the cut-in wind speed, the effective damping of the system becomes negative, and the system starts to lose stability and carries on self-excited oscillation. With the increase of wind speed, the magnitude of the effective negative damping increases, the power output from the coupled energy transducer becomes larger. Hence, a galloping-based energy harvester can operate over a wide wind speed range. For these advantages, immense efforts have been devoted to promoting the development of galloping-based energy harvesting in the past decade (Barrero-Gil et al., 2010, 2020; Ewere et al., 2014; Sirohi and Mahadik, 2012; Tan et al., 2019).

A typical galloping-based energy harvesting can be achieved by attaching a bluff body to a classic cantilever beam based VEH. When immersed in the wind flow, the bluff body incurs the aerodynamic force and plays the role of the input excitation. Therefore, the bluff body undoubtedly has an essential effect on the energy harvesting performance. Yang et al. (2013) compared various sectioned bluff bodies in an experimental study and found that using a square-sectioned bluff body could lead to higher power output. Apart from the research of modifying bluff bodies to improve the energy harvesting performance (Liu et al., 2019a; Wang et al., 2019b), the evolution of galloping-based energy harvester is very similar to the track of the development of its predecessor, that is, vibration energy harvester: from linear (Barrero-Gil et al., 2010; Yang et al., 2013) to nonlinear design (Bibo et al., 2015b; Wang et al., 2020b; Zhao and Yang, 2018), and from single-degree-of-freedom (SDOF) (Barrero-Gil et al., 2010; Sirohi and Mahadik, 2011, 2012) to multiple-degree-of-freedom (MDOF) design (Hu et al., 2021a, 2021b; Lan et al., 2019; Zhao et al., 2014).

In addition to following the track of vibration energy harvester development, researchers proposed integrating them to harvest energy from concurrent wind and base excitation in the recent few years. Bibo and Daqaq (2013b) presented a pioneering work to investigate a flutter energy harvester under combined wind and base excitations. The method of normal forms was applied to derive the approximate solution of the voltage response from the flutter energy

harvester. A later work by them presented the corresponding experimental study of the proposed flutter energy harvester under the combined excitation (Bibo and Daqaq, 2013a). Dai et al. (2014) studied a piezoelectric energy harvester (PEH) subjected to concurrent vortex-induced vibration (VIV) and base excitation through simulations and experiments. However, the analytical solution to the VIV-based PEH under dual-exitations was not presented. Following the same idea, Yan et al. (2014) and Bibo et al. (2015a) explored galloping-based energy harvesters under concurrent wind and base excitation by simulation and experimental studies. Zhao and Yang (2018) and Zhao (2020) then introduced mechanical stoppers and magnetic bistable nonlinearity into a galloping-based energy harvester under concurrent excitation to achieve broadband ability based on experiments and simulations. Analytical solutions for the mechanical and electrical responses were derived based on harmonic balance method for the bistable system under concurrent galloping and base excitation [39]. Zhao (2020) also derived the analytical solution for the stopper integrated piecewise-linear galloping-based PEH under concurrent wind and base excitation based on the averaging method. The decoupling treatment greatly simplified the mathematical problem.

According to the literature review, the research in the field of concurrent wind and base excitation energy harvesting is at the emerging stage. Existing research of concurrent energy harvesting is still limited to SDOF system designs. As is well-known, multiple-degree-of-freedom systems have multiple resonant peaks (Tang and Yang, 2012). In this paper, a two-degree-of-freedom (2DOF) galloping-based piezoelectric energy harvester (GPEH) is considered to cover a wider frequency spectrum for energy harvesting. The approximate analytical solution of the system is derived using the harmonic balance method. An equivalent circuit model based on the electro-mechanical analogies is established to verify the analytical solution. Phenomena such as quasi-periodic oscillations due to concurrent excitation, peak-to-valley transition in frequency response are successfully explained by the analytical solution. This work aims to provide some theoretical guidelines in analyzing such kind of energy harvesters under concurrent excitation. The analysis procedures presented in this paper can be easily applied for other SDOF or multiple-DOF GPEHs under concurrent aeroelastic and base excitation. It is worth mentioning that Hu et al. (2022) studied a similar 2DOF GPEH model as presented in this paper. However, only the wind load is considered in that work, which indicates a simpler excitation condition. Compared to the study presented in that paper, the mathematical treatments adopted in deriving the

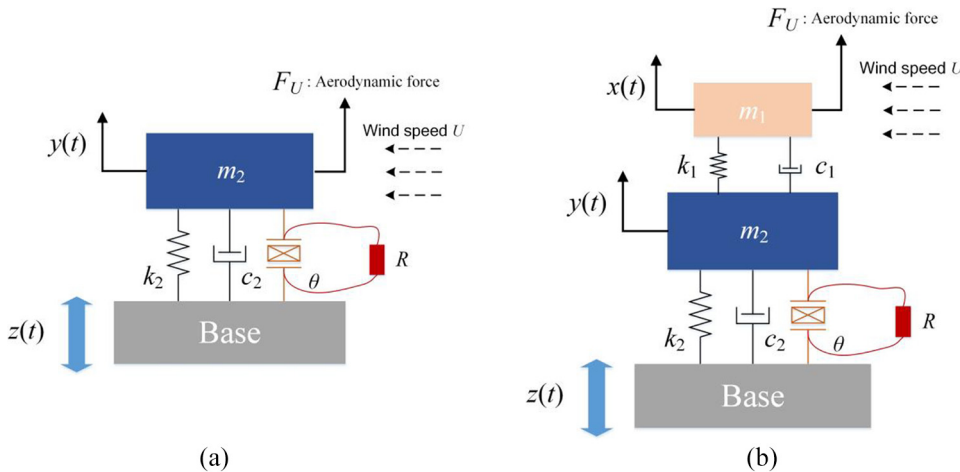


Figure 1. Schematic of (a) the SDOF and (b) the 2DOF piezoelectric energy harvester under concurrent aeroelastic and base excitation.

analytical solutions are not the same, and the consequent phenomena are different.

2. Aero-electro-mechanical model

Figure 1(a) shows the schematic of a SDOF PEH under concurrent aeroelastic and base excitation. Relevant studies of such kind of SDOF PEH can be found in the literature (Zhao, 2020; Zhao and Yang, 2018). Figure 1(b) shows the schematic of the proposed 2DOF PEH under concurrent aeroelastic and base excitation. The 2DOF PEH consists of a primary oscillator and an auxiliary oscillator. The primary oscillator is directly connected to the base. A piezoelectric transducer is coupled with the primary oscillator to realize energy transduction. The whole structure is placed in a wind flow field. The auxiliary oscillator is equipped with a bluff body where the aerodynamic force is applied. The dimension of the primary oscillator is assumed to be small compared to the bluff body attached to the auxiliary oscillator; thus, the aerodynamic force acting on the primary oscillator is reasonably considered to be negligible.

By representing the aerodynamic force as a third-order polynomial function (Abdelmoula and Abdelkefi, 2017; Javed and Abdelkefi, 2017), the governing equations of the 2DOF PEH, as shown in Figure 1, can be written as:

$$m_1 \ddot{x}(t) + c_1 (\dot{x}(t) - \dot{y}(t)) + k_1 (x(t) - y(t)) = \frac{1}{2} \rho U^2 L D_B \left(s_1 \frac{\dot{x}(t)}{U} - s_3 \left(\frac{\dot{x}(t)}{U} \right)^3 \right) \quad (1)$$

$$m_2 \ddot{y}(t) + c_2 (\dot{y}(t) - \dot{z}(t)) + k_2 (y(t) - z(t)) + c_1 (\dot{y}(t) - \dot{x}(t)) + k_1 (y(t) - x(t)) + \theta v(t) = 0 \quad (2)$$

$$C_p \dot{v}(t) + \frac{v(t)}{R} = \theta (\dot{y}(t) - \dot{z}(t)) \quad (3)$$

where \$m_i\$, \$c_i\$, and \$k_i\$ severally represent the mass, the damping coefficient, and the stiffness of the oscillator. The subscript \$i = 1\$ and \$2\$ denote the auxiliary and the primary oscillators, respectively. \$x(t)\$ and \$y(t)\$ are the absolute displacements of the primary and the auxiliary oscillators, respectively. \$z(t)\$ is the displacement of the base. \$\rho\$ is the air density and \$U\$ is the wind speed. \$s_1\$ and \$s_3\$ are the empirical linear and cubic coefficients of the transverse galloping force. The characteristic area of the bluff body normal to the wind flow is \$L \times D_B\$. \$\theta\$ and \$C_p\$ are the electro-mechanical coupling coefficient and the clamped capacitance of the piezoelectric transducer, respectively. \$v(t)\$ is the voltage across the load resistance \$R\$.

3. Approximate analytical solution

Without loss of generality, the base excitation is considered to be in the form as:

$$z(t) = Z_b \sin(\omega_b t) \quad (4)$$

where \$\omega_b\$ is the angular frequency of the base excitation. Since the 2DOF PEH is under the concurrent aeroelastic and base excitation, the displacement response of the auxiliary oscillator may be the combination of two components: one is the forced vibration component with the frequency of the base excitation and the other is the limited cycle oscillation component with the fundamental natural frequency of the 2DOF PEH (Lan et al., 2019). The solution to the displacement of the auxiliary oscillator is assumed to be the superposition of these two components.

$$x(t) = x_b(t) + x_g(t) \quad (5)$$

where the subscripts b and g denote the base excitation induced component and the galloping induced component, respectively. To be more specific, they can be expanded as:

$$x_b(t) = a_1(t) \sin(\omega_b t) + b_1(t) \cos(\omega_b t) \quad (6)$$

$$x_g(t) = g_1(t) \sin(\omega_g t) + h_1(t) \cos(\omega_g t) \quad (7)$$

where ω_g is the angular frequency of the limited cycle oscillation induced by galloping. For the same reason, the displacement of the primary oscillator is also assumed in the form as the superposition of two components:

$$y(t) = y_b(t) + y_g(t) \quad (8)$$

Each component can be further detailed as:

$$y_b(t) = a_2(t) \sin(\omega_b t) + b_2(t) \cos(\omega_b t) \quad (9)$$

$$y_g(t) = g_2(t) \sin(\omega_g t) + h_2(t) \cos(\omega_g t) \quad (10)$$

Similarly, the same assumption is applied to the voltage response.

$$v(t) = v_b(t) + v_g(t) \quad (11)$$

$$v_b(t) = v_1(t) \sin(\omega_b t) + v_2(t) \cos(\omega_b t) \quad (12)$$

$$v_g(t) = v_3(t) \sin(\omega_g t) + v_4(t) \cos(\omega_g t) \quad (13)$$

The amplitudes of the response components are defined as:

$$\begin{cases} (r_{11}(t))^2 = (a_1(t))^2 + (b_1(t))^2 & (r_{21}(t))^2 = (a_2(t))^2 \\ & + (b_2(t))^2 \\ (r_{12}(t))^2 = (g_1(t))^2 + (h_1(t))^2 & (r_{22}(t))^2 = (g_2(t))^2 \\ & + (h_2(t))^2 \\ (V_b(t))^2 = (v_1(t))^2 + (v_2(t))^2 & (V_g(t))^2 = (v_3(t))^2 \\ & + (v_4(t))^2 \end{cases} \quad (14)$$

Before directly starting to solve the governing equations, one may have noticed that equation (3) does not involve any nonlinearities and contains only two unknown variables, that is, $y(t)$ and $v(t)$. Therefore, it is motivated to find the linear relationship between $y(t)$ and $v(t)$ through equation (3) and represent $v(t)$ by $y(t)$ to eliminate one unknown variable. In this way, the number of the governing equations can be reduced, and the problem can be greatly simplified. To this end, we first substitute equations (8) and (11) into equation (3), then abandon the higher harmonics and balance the terms of $\sin(\omega_b t)$, $\cos(\omega_b t)$, $\sin(\omega_g t)$, and $\cos(\omega_g t)$. Consequently, we obtain four equations, as follows:

$$\begin{cases} -C_p v_2(t) \omega_b + \frac{v_1(t)}{R} + \theta b_2(t) \omega_b = 0 \\ C_p v_1(t) \omega_b + \frac{v_2(t)}{R} - \theta a_2(t) \omega_b + \theta Z_b \omega_b = 0 \\ -C_p v_4(t) \omega_g + \frac{v_3(t)}{R} + \theta h_2(t) \omega_g = 0 \\ C_p v_3(t) \omega_g + \frac{v_4(t)}{R} - \theta g_2(t) \omega_g = 0 \end{cases} \quad (15)$$

Based on equation (15), one can solve $v_1(t) \sim v_4(t)$ and represent them using $a_2(t) \sim g_2(t)$:

$$\begin{cases} v_1(t) = \frac{K_{e1} a_2(t)}{\theta} - \frac{C_{e1} b_2(t)}{\theta} - \frac{K_{e1} Z_b}{\theta} \\ v_2(t) = \frac{C_{e1} a_2(t)}{\theta} + \frac{K_{e1} b_2(t)}{\theta} - \frac{C_{e1} Z_b}{\theta} \\ v_3(t) = \frac{K_{e2} g_2(t)}{\theta} - \frac{C_{e2} h_2(t)}{\theta} \\ v_4(t) = \frac{C_{e2} g_2(t)}{\theta} + \frac{K_{e2} h_2(t)}{\theta} \end{cases} \quad (16)$$

where $K_{e1} = \frac{R^2 \theta^2 \omega_b^2 C_p}{C_p^2 R^2 \omega_b^2 + 1}$, $C_{e1} = \frac{R \theta^2 \omega_b}{C_p^2 R^2 \omega_b^2 + 1}$, $K_{e2} = \frac{R^2 \theta^2 \omega_g^2 C_p}{C_p^2 R^2 \omega_g^2 + 1}$, and $C_{e2} = \frac{R \theta^2 \omega_g}{C_p^2 R^2 \omega_g^2 + 1}$. Hence, the voltage response can be expressed using $y_b(t)$ and $y_g(t)$.

$$\begin{aligned} v(t) = & \frac{K_{e1} y_b(t)}{\theta} + \frac{K_{e2} y_g(t)}{\theta} - \frac{K_{e1} z(t)}{\theta} + \frac{C_{e1} \dot{y}_b(t)}{\theta \omega_b} \\ & + \frac{C_{e2} \dot{y}_g(t)}{\theta \omega_g} - \frac{C_{e1} \dot{z}(t)}{\theta \omega_b} \end{aligned} \quad (17)$$

One can then eliminate the unknown variable $v(t)$ in equation (2) by substituting equation (17) into it, and focus on the governing equations that are constituted of equations (1) and (2) only. Substituting equations (5) and (8) into equations (1) and (2), balancing the coefficients of the terms $\sin(\omega_b t)$ and $\cos(\omega_b t)$, respectively, and making simplifications using equation (14), one obtains the following four equations:

$$\begin{aligned} & (-m_1 \omega_b^2 + k_1) a_1(t) + c_1 b_2(t) \omega_b - c_1 \omega_b b_1(t) - k_1 a_2(t) \\ & = \frac{b_1(t)}{8U} (3 D_B L \rho s_3 \omega_b^3 (r_{11}(t))^2 + 6 D_B L \rho s_3 \omega_b \omega_g^2 \\ & \quad (r_{12}(t))^2 - 4 U^2 \rho L D_B s_1 \omega_b) \end{aligned} \quad (18)$$

$$\begin{aligned} & c_1 a_1(t) \omega_b - c_1 a_2(t) \omega_b + (-m_1 \omega_b^2 + k_1) b_1(t) - k_1 b_2(t) \\ & = \frac{a_1(t)}{8U} (-3 D_B L \rho s_3 \omega_b^3 (r_{11}(t))^2 - 6 D_B L \rho s_3 \omega_b \omega_g^2 \\ & \quad (r_{12}(t))^2 + 4 U^2 \rho L D_B s_1 \omega_b) \end{aligned} \quad (19)$$

$$\begin{aligned} & (-m_2 \omega_b^2 + K_{e1} + k_2) a_2(t) + (-c_2 \omega_b - C_{e1}) b_2(t) \\ & - (K_{e1} + k_2) Z_b \\ & = -c_1 \omega_b b_1(t) + c_1 b_2(t) \omega_b + k_1 a_1(t) - k_1 a_2(t) \end{aligned} \quad (20)$$

$$\begin{aligned} & (c_2 \omega_b + C_{e1}) a_2(t) + (-m_2 \omega_b^2 + K_{e1} + k_2) b_2(t) \\ & - (\omega_b c_2 + C_{e1}) Z_b \\ & = c_1 a_1(t) \omega_b - c_1 a_2(t) \omega_b + k_1 b_1(t) - k_1 b_2(t) \end{aligned} \quad (21)$$

It is worth noting that the derivatives of the unknown variables are forced to be zeros, as the steady-state solutions are to be sought. In other words, the steady-state solutions of the amplitudes are supposed to be constants. Hence, the time dependency is omitted hereinafter, for example, $a_1(t) \rightarrow a_1$, $r_{11}(t) \rightarrow r_{11}$. Based on equations (20) and (21), we can represent a_2 and b_2 by a_1 and b_1 :

$$\begin{cases} a_2 = P_1 a_1 + Q_1 b_1 + O_1 \\ b_2 = -Q_1 a_1 + P_1 b_1 - O_2 \end{cases} \quad (22)$$

where the definitions of P_1 , Q_1 , O_1 , and O_2 are given in the Appendix. Substituting equation (22) into equations (18) and (19), respectively, yields equations (23) and (24):

$$\begin{aligned} & (-Q_1 c_1 \omega_b - m_1 \omega_b^2 - P_1 k_1 + k_1) a_1 + (P_1 c_1 \omega_b - Q_1 k_1 - c_1 \omega_b) b_1 - c_1 \omega_b O_2 - k_1 O_1 \\ & = \left(\frac{3}{8} \frac{D_B L \rho s_3 \omega_b^3 r_{11}^2}{U} + \frac{3}{4} \frac{D_B L \rho s_3 \omega_b \omega_g^2 r_{12}^2}{U} - \frac{1}{2} U \rho L D_B s_1 \omega_b \right) b_1 \end{aligned} \quad (23)$$

$$\begin{aligned} & (-P_1 c_1 \omega_b + Q_1 k_1 + c_1 \omega_b) a_1 + (-Q_1 c_1 \omega_b - m_1 \omega_b^2 - P_1 k_1 + k_1) b_1 - c_1 \omega_b O_1 + k_1 O_2 \\ & = \left(-\frac{3}{8} \frac{D_B L \rho s_3 \omega_b^3 r_{11}^2}{U} - \frac{3}{4} \frac{D_B L \rho s_3 \omega_b \omega_g^2 r_{12}^2}{U} + \frac{1}{2} U \rho L D_B s_1 \omega_b \right) a_1 \end{aligned} \quad (24)$$

Solving equations (23), (24), and (14) simultaneously, one can vanish a_1 and b_1 and obtain:

$$\begin{aligned} & -576 D_B^2 L^2 \rho^2 s_3^2 \omega_b^6 r_{11}^6 + 1536 D_B L s_3 \left(\frac{-3/2 L s_3 \omega_b \omega_g^2 \rho D_B r_{12}^2}{U (U \rho L D_B s_1 \omega_b + 2 c_1 (P_1 - 1) \omega_b - 2 Q_1 k_1)} \right) \rho \omega_b^3 r_{11}^4 \\ & + \left(-2304 D_B^2 L^2 \rho^2 s_3^2 \omega_b^2 \omega_g^4 r_{12}^4 + 3072 U \left(\frac{U \rho L D_B s_1 \omega_b}{+ 2 c_1 (P_1 - 1) \omega_b} \right) D_B \omega_g^2 L s_3 \rho \omega_b r_{12}^2 \right. \\ & \left. + \left(-1024 U^2 \left(\frac{L^2 s_1^2 \omega_b^2 U^2 \rho^2 D_B^2 + 4 D_B (c_1 (P_1 - 1) \omega_b - Q_1 k_1) L \rho s_1 \omega_b U}{+ 4 m_1^2 \omega_b^4 + 8 Q_1 c_1 m_1 \omega_b^3 + ((4 P_1^2 + 4 Q_1^2 - 8 P_1 + 4) c_1^2 + 8 k_1 m_1 (P_1 - 1)) \omega_b^2 + 4 k_1^2 (P_1^2 + Q_1^2 - 2 P_1 + 1)} \right) \right) r_{11}^2 \right. \\ & \left. + 4096 U^2 (O_1^2 + O_2^2) (c_1^2 \omega_b^2 + k_1^2) = 0 \right) \end{aligned} \quad (25)$$

which is an equation that contains only two unknown variables r_{11} and r_{12} . To make the problem solvable, one more equation that describes the relationship

between r_{11} and r_{12} is to be sought. Moreover, one also obtains the expressions of a_1 and b_1 by r_{11} and r_{12} . The detailed expressions of a_1 and b_1 as the functions of r_{11} and r_{12} are given in the Appendix. On the other hand, after substituting equations (5) and (8) into equations (1) and (2), one can choose to balance the coefficients of the terms $\sin(\omega_g t)$ and $\cos(\omega_g t)$. Consequently, the following four equations are obtained:

$$\begin{aligned} & (-m_1 \omega_g^2 + k_1) g_1 - \omega_g c_1 h_1 + \omega_g c_1 h_2 - k_1 g_2 \\ & = \frac{h_1}{8U} (3 D_B L \rho s_3 \omega_g^3 r_{12}^2 + 6 D_B L \rho s_3 \omega_b^2 \omega_g r_{11}^2 - 4 D_B L U^2 \rho s_1 \omega_g) \end{aligned} \quad (26)$$

$$\begin{aligned} & -\omega_g^2 m_1 h_1 + \omega_g c_1 g_1 - \omega_g c_1 g_2 + k_1 h_1 - k_1 h_2 \\ & = \frac{g_1}{8U} (-6 D_B L \rho s_3 \omega_b^2 \omega_g r_{11}^2 - 3 D_B L \rho s_3 \omega_g^3 r_{12}^2 + 4 D_B L U^2 \rho s_1 \omega_g) \end{aligned} \quad (27)$$

$$\begin{aligned} & k_2 g_2 - \omega_g^2 m_2 g_2 - \omega_g c_2 h_2 - C_{e2} h_2 + K_{e2} g_2 \\ & = -\omega_g c_1 h_1 + \omega_g c_1 h_2 + k_1 g_1 - k_1 g_2 \end{aligned} \quad (28)$$

$$\begin{aligned} & k_2 h_2 - \omega_g^2 m_2 h_2 + \omega_g c_2 g_2 + C_{e2} g_2 + K_{e2} h_2 \\ & = \omega_g c_1 g_1 - \omega_g c_1 g_2 + k_1 h_1 - k_1 h_2 \end{aligned} \quad (29)$$

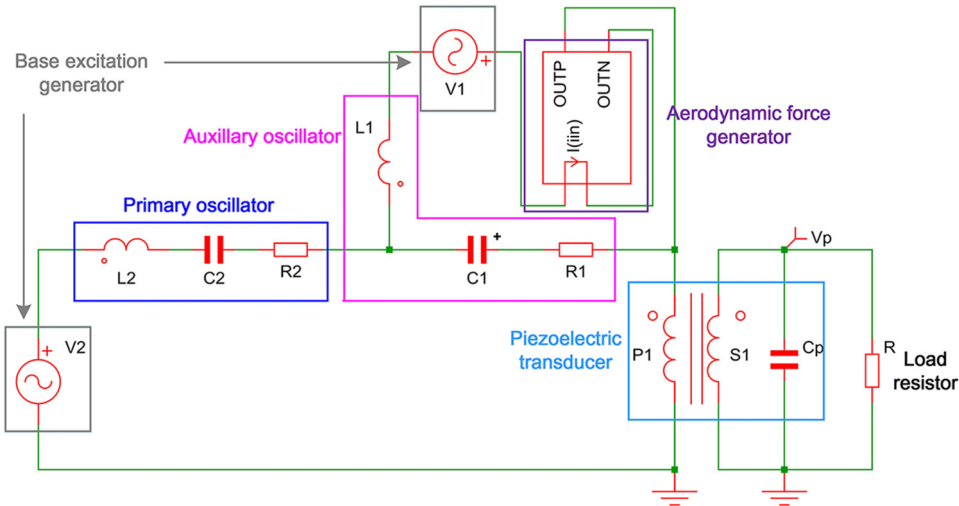


Figure 2. Equivalent circuit model of the 2DOF PEH established in SIMetrix.

According to equations (28) and (29), we can represent g_2 and h_2 by g_1 and h_1 :

$$\begin{cases} g_2 = \Gamma_1 g_1 + \Gamma_2 h_1 \\ h_2 = -\Gamma_2 g_1 + \Gamma_1 h_1 \end{cases} \quad (30)$$

where the definitions of Γ_1 , Γ_2 , Γ_3 , and Γ_4 are provided in the Appendix. Substituting equation (30) into equations (26) and (27), respectively, produces:

$$\begin{aligned} & (-c_1\Gamma_2\omega_g - m_1\omega_g^2 - k_1\Gamma_1 + k_1)g_1 + (c_1\Gamma_1\omega_g - c_1\omega_g - k_1\Gamma_2)h_1 \\ &= \frac{h_1}{8U} (3D_B L\rho s_3 \omega_g^3 r_{12}^2 + 6D_B L\rho s_3 \omega_b^2 \omega_g r_{11}^2 - 4D_B L U^2 \rho s_1 \omega_g) \end{aligned} \quad (31)$$

$$\begin{aligned} & (-c_1\Gamma_1\omega_g + c_1\omega_g + k_1\Gamma_2)g_1 + (-c_1\Gamma_2\omega_g - m_1\omega_g^2 - k_1\Gamma_1 + k_1)h_1 \\ &= \frac{g_1}{8U} (-6D_B L\rho s_3 \omega_b^2 \omega_g r_{11}^2 - 3D_B L\rho s_3 \omega_g^3 r_{12}^2 + 4D_B L U^2 \rho s_1 \omega_g) \end{aligned} \quad (32)$$

By subtracting equation (31) $\times h_1$ by equation (32) $\times g_1$, then using the definitions in equation (14), the unknown variables g_1 and h_1 can be eliminated and another equation that involves the relationship between r_{11} and r_{12} is obtained.

$$\begin{aligned} & (c_1\Gamma_1\omega_g - c_1\omega_g - k_1\Gamma_2)r_{12}^2 \\ &= \frac{1}{8U} (3D_B L\rho s_3 \omega_g^3 r_{12}^4 + 6D_B L\rho s_3 \omega_b^2 \omega_g r_{11}^2 r_{12}^2) \\ &- 4D_B L U^2 \rho s_1 \omega_g r_{12}^2 \end{aligned} \quad (33)$$

Therefore, by solving equations (25) and (33) simultaneously, the solutions to r_{11} and r_{12} can be finally derived. After deriving r_{11} and r_{12} , one can use the equations in the Appendix to calculate a_1 and b_1 . Moreover, based on equation (31) and the definition that $r_{12}^2 = g_1^2 + h_1^2$, one can solve g_1 and h_1 as well. Their detailed expressions are given in the Appendix. Subsequently, using equations (22) and (30), a_1 , b_1 , g_1 ,

and h_1 can be computed, thus r_{21} and r_{22} . Finally, the voltage response can be solved based on equation (16), and the voltage amplitudes can be expressed using r_{21} and r_{22} as:

$$\begin{cases} V_a = \frac{1}{\theta} \sqrt{(C_{e1}^2 + K_{e1}^2)(r_{21}^2 - 2Z_b a_2 + Z_b^2)} \\ V_b = \frac{r_{22}}{\theta} \sqrt{(C_{e2}^2 + K_{e2}^2)} \end{cases} \quad (34)$$

Since the voltage response may consist of two harmonic components with different frequencies, the maximum voltage amplitude is not suitable to be directly used as a figure of merit to evaluate the energy harvesting performance anymore. To this end, the root-mean-square (RMS) voltage is used to measure the actual magnitude.

$$V_{RMS} = \sqrt{\frac{1}{2T} \int_{-T}^T [v_1(t) \sin(\omega_b t) + v_2(t) \cos(\omega_b t) + v_3(t) \sin(\omega_g t) + v_4(t) \cos(\omega_g t)]^2 dt} \quad (35)$$

where T is the period of repetition. However, due to the complexity of the dual-frequency response, the accurate T can not be easily determined. As an alternative and convenient numerical means, one can use a large time period instead. When T is sufficiently large, the result infinitely approaches the actual V_{RMS} . For harmonic response components at ω_b and ω_g , the RMS voltage is simply (rms of sum of trigometric functions):

$$V_{RMS} = \sqrt{\frac{V_a^2 + V_b^2}{2}} \quad (36)$$

4. Equivalent circuit model

An equivalent circuit model (ECM) shown in Figure 2 is built in the commercial software SIMetrix to verify

Table I. Mechanical and aerodynamic parameters of the 2DOF PEH under investigation.

Electro-mechanical parameters			
Effective mass m_1 (g)	113.4	Damping ratio ζ_2	0.003
Effective mass m_2 (g)	113.4	Electromechanical coupling θ ($\mu\text{N/V}$)	190
Effective stiffness k_1 (N/m)	58.02	Capacitance C_p (nF)	187
Effective stiffness k_2 (N/m)	58.02	Load resistance R (Ω)	10^{12}
Damping ratio ζ_1	0.003		

Aerodynamic parameters			
Air density, ρ (kg/m^3)	1.24	Bluff body height, L (m)	0.1
Cross flow dimension, D_B (m)	0.05	Linear aerodynamic coefficient, s_1	2.5
Cubic aerodynamic coefficient, s_3	130	Wind speed U (m/s)	varying

the derived analytical solution of the 2DOF PEH under concurrent aeroelastic and base excitation. To establish the equivalent circuit model, based on the electro-mechanical analogies, the mechanical quantities are first converted into the equivalent electrical quantities: force and velocity are equivalent to voltage and current, respectively. The mechanical elements such as mass, spring, and damper are equivalent to the electrical elements as the inductor, capacitor, and resistor, respectively. The piezoelectric transducer can be equivalently represented by the combination of an ideal transformer and a capacitor.

According to the above principles, the mechanical domain of the 2DOF PEH is converted into the equivalent circuit on the left-hand side of Figure 2, consisting of two loops squared by blue and pink blocks. Each circuit loop represents each oscillator. The mappings between the values of the electrical elements and the corresponding mechanical elements are:

$$\begin{aligned} L_1 &= m_1; \quad R_1 = c_1; \quad C_1 = 1/k_1; \quad V_1 = -m_1\ddot{z}(t) \\ L_2 &= m_2; \quad R_2 = c_2; \quad C_2 = 1/k_2; \quad V_2 = -m_2\ddot{z}(t) \end{aligned} \quad (37)$$

The piezoelectric transducer plays the role of bridging the mechanical and electrical domains. The wing ratio of the ideal transformer that equals $1:\theta$ reflects the electro-mechanical coupling strength of the piezoelectric transducer. The true interface circuit can then be directly connected to the right-hand side of the ideal transformer in parallel with the capacitor C_p . The aerodynamic force can be implemented by a nonlinear transfer function in SIMetrix. To be more specific, a voltage source (i.e. the galloping-induced force) can be defined as the function of the current (i.e. vibration velocity $\dot{x}(t)$) flowing out of the circuit loop that represents the auxiliary oscillator. In the circuit simulation, a transient analysis should be performed for a sufficiently long time until the circuit reaches steady-state. The voltage response across the load resistor R can be straightforwardly measured by placing a voltage probe. More

detailed procedures can be referred to the similar works in the existing literature (Tang et al., 2015; Wang et al., 2020c).

5. Results and discussion

In this section, a specific 2DOF PEH is considered. No study of 2DOF PEH under combined excitations has ever been reported. This paper focuses on the theoretical study to provide some preliminary insights. The system parameter listed in Table 1 are taken from Lan et al. (2019), in which a 2DOF PEH under only the wind excitation is investigated. It is worth noting that though the model presented in Lan et al. (2019) is similar, the existence of the combined excitations considered in this paper makes the problem become much more complicated. For example, it will be shown that a quasi-periodic oscillation phenomenon and a quenching phenomenon may appear in the following case studies. For the given parameters listed in Table 1, the first and the second natural frequencies of the 2DOF PEH are, respectively, $f_1 = 2.23$ Hz and $f_2 = 5.83$ Hz. The wind speed U is varied to investigate its effect on the dynamic response of the 2DOF PEH. The analytical results are compared with the circuit simulation results for verification.

For the given 2DOF PEH under the base excitation with a constant acceleration amplitude of $A_{cc} = 1$ m/ s^2 , Figure 3(a) shows the analytically predicted voltage amplitudes of V_b and V_g versus the wind speed U and the non-dimensionless frequency f/f_1 . Figure 3(b) shows the corresponding RMS voltage evolution. The results of a conventional SDOF PEH under the combined excitation are also illustrated in Figure 3 for comparison. First of all, it can be seen that both SDOF and 2DOF PEHs have similar evolution behaviors. Compared to the SDOF PEH, it is noted that the V_b component of the 2DOF PEH is always larger. When deviating away from the resonance state $f/f_1 \approx 1$, the V_g component of the SDOF PEH is first larger, but later becomes smaller than that of the 2DOF PEH. As the

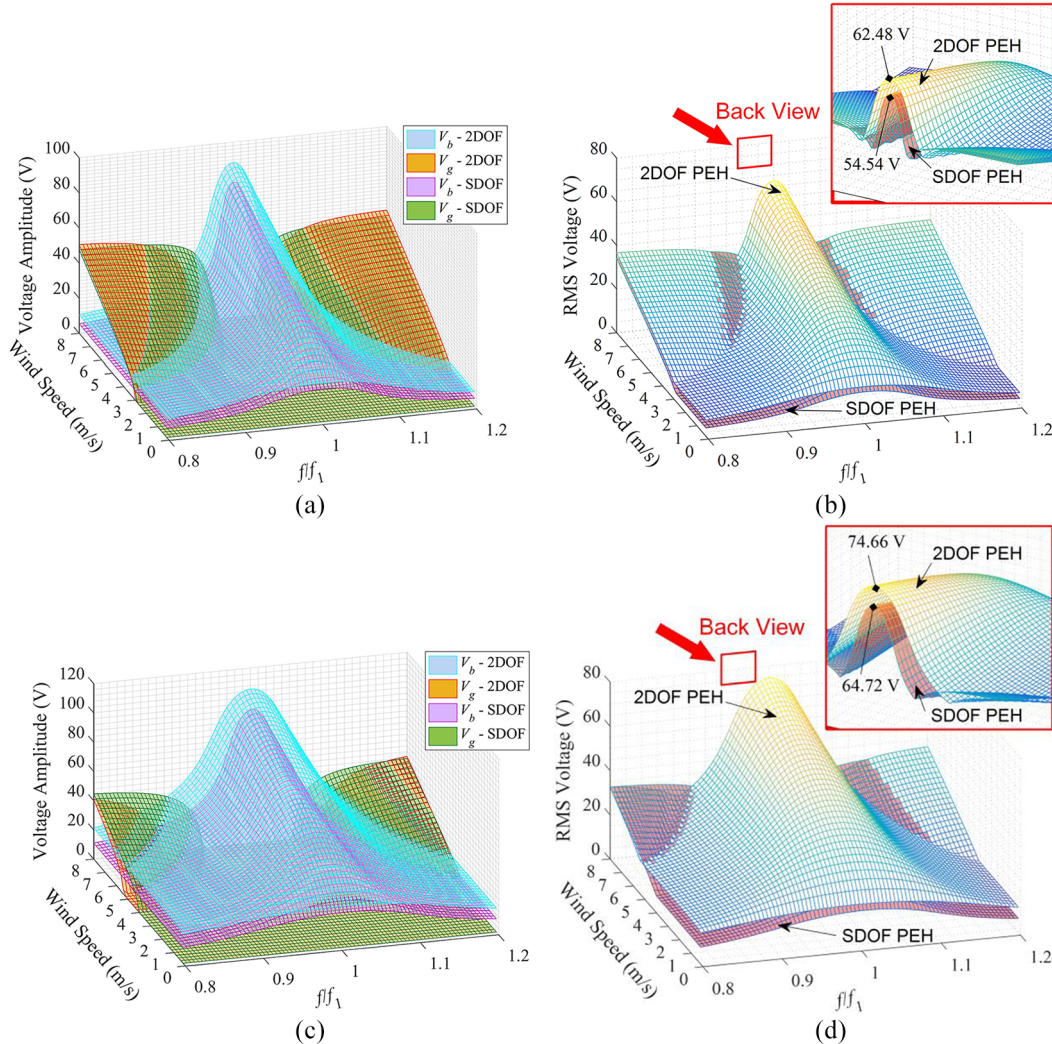


Figure 3. Analytically obtained voltage amplitudes of V_b and V_g versus wind speed U and the non-dimensionless frequency f/f_1 : (a) $A_{cc} = 1 \text{ m/s}^2$ and (c) $A_{cc} = 2 \text{ m/s}^2$; RMS voltage versus wind speed U and the non-dimensionless frequency f/f_1 : (b) $A_{cc} = 1 \text{ m/s}^2$ and (d) $A_{cc} = 2 \text{ m/s}^2$.

maximum voltage is achieved near the resonance state and the main output is contributed by the V_b component, the 2DOF PEH exhibits a better energy harvesting performance due to a higher voltage output.

Since the evolution behaviors of both PEHs are similar and the performance of the 2DOF PEH is found to be better, we focus on the behavior of the 2DOF PEH hereinafter. It can be seen that when the wind speed is low, V_g constantly equals zero, which indicates the inactivation of the galloping-induced vibration. With the increase of the wind speed and after it exceeds a critical value, that is, the cut-in wind speed, V_g becomes non-zero and starts to increase monotonically. Moreover, it is noted that when the excitation frequency is different, the cut-in wind speed is different. In particular, when the excitation frequency deviates farther away from the fundamental resonant frequency of the 2DOF PEH,

that is, $f/f_1 = 1$, the cut-in wind speed becomes smaller. Therefore, from the perspective of low-wind speed galloping energy harvesting, it is known that the existence of the base excitation is undesirable.

The contributions of the galloping-induced vibration and the forced vibration by base excitation on the actual voltage output of the 2DOF PEH around the fundamental resonant frequency is reflected through comparing Figure 3(a) and (b). It is learned that when the excitation frequency is near the fundamental resonant frequency of the 2DOF PEH, V_g becomes 0 and the main contribution comes from the base excitation, which is the typical quenching phenomenon (Abdelmoula and Abdelkefi, 2017). However, when the excitation frequency mismatches with the fundamental resonant frequency evidently, V_g becomes significantly larger than V_b , which implies that the wind excitation starts to

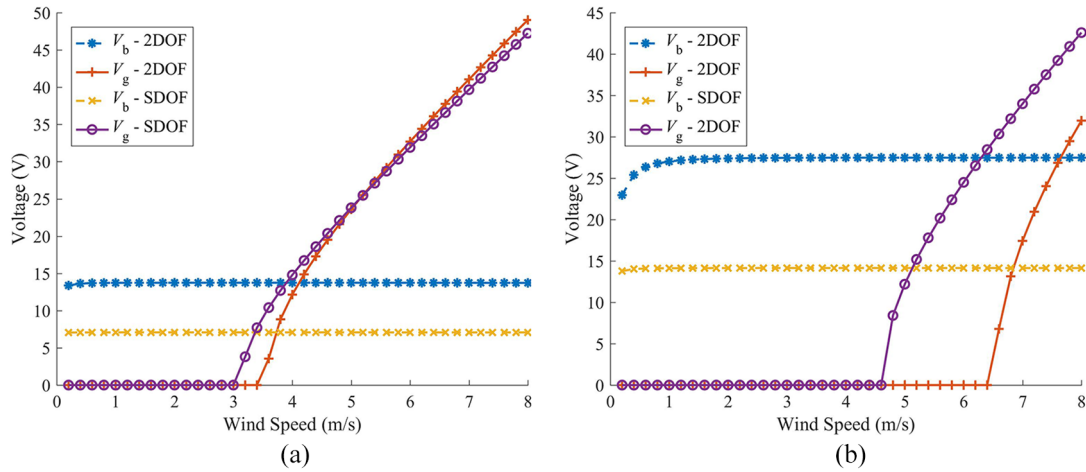


Figure 4. Given the base excitation frequency of $f/f_1 = 0.85$, the analytically obtained voltage amplitudes of V_b and V_g versus the wind speed: (a) $A_{cc} = 1 \text{ m/s}^2$ and (b) $A_{cc} = 2 \text{ m/s}^2$.

replace the role of base excitation and becomes the principal source for the 2DOF PEH to realize energy transduction.

The base excitation level is then increased to 2 m/s^2 to examine its influence on the energy harvesting performance of the 2DOF PEH around the fundamental resonance. The updated voltage amplitudes and RMS voltage are presented in Figure 3(c) and (d), respectively. As compared with the results in Figure 3(a), it is found in Figure 3(c) that the increase of the base excitation weakens the galloping-induced vibration, that is, V_g decreases globally. Additionally, the increase of the base excitation also raises the threshold of the activation of galloping-induced vibration. In other words, the quenching region becomes wider with the increase of the base excitation (Abdelmoula and Abdelkefi, 2017; Yan et al., 2018). This further confirms the previous statement that base excitation is unfavorable from the perspective of galloping energy harvesting.

To better present the information that might be difficult to be captured in Figure 3, such as the Hopf bifurcation phenomenon, a 2D graph, that is, Figure 4, plots the analytically obtained voltage amplitudes of V_b and V_g versus the wind speed at the given base excitation frequency of $f/f_1 = 0.85$. It can be seen that when the wind speed is small, the 2DOF PEH vibrates due to the base excitation, that is, $V_g = 0$. As the wind speed increases, the system undergoes Hopf bifurcation, and galloping appears. Moreover, by comparing Figure 4(a) and (b), it is found that with the increase of the base excitation, the base excitation-induced voltage output, that is, V_b , becomes larger. While the galloping-induced voltage output, that is, V_g , becomes smaller.

The interest is then turned to the energy harvesting performance of the 2DOF PEH around its second resonant frequency. Under the base excitation of $A_{cc} = 1 \text{ m/s}^2$, by varying the wind speed and the

excitation frequency around f_2 , Figure 5(a) and (b) illustrate the evolutions of the voltage amplitudes of V_b and V_g and the RMS voltage, respectively. From Figure 5(a), it can be seen that when the wind speed is low, the galloping phenomenon unsurprisingly can not be incurred, that is, $V_g = 0$. As compared with Figure 3(a), the cut-in wind speed of the 2DOF PEH overall decreases, which is beneficial for low-speed wind energy harvesting. Moreover, under the same wind speed, V_g around the second resonance of the 2DOF PEH, as shown in Figure 5(a), becomes generally larger than the result presented in Figure 3(a). Hence, it can be reasonably deduced that with the increase of the excitation frequency, from only the galloping energy harvesting point of view, the performance is improved.

On the other hand, regarding the overall energy harvesting performance, which is revealed by the RMS voltage output as shown in Figure 5(b), it is noted that the peak at the second resonant frequency strangely becomes a valley with the increase of the wind speed. Such a peak-to-valley transition phenomenon goes against common sense based on the knowledge and experience of classic dynamic systems, which tell us that there should appear peaks in the frequency responses at the resonant frequencies. A more detailed discussion about this abnormal phenomenon will be provided later, together with the numerical verification. Due to this phenomenon, it should be aware that the second resonance can not always benefit energy harvesting anymore. Especially under the high wind speed, the base excitation frequency even should be away from the second resonant frequency of the 2DOF PEH to achieve a high efficiency.

Similarly, the base excitation is then increased to 2 m/s^2 to see the consequence. Figure 5(c) and (d) present the corresponding results of the voltage amplitudes

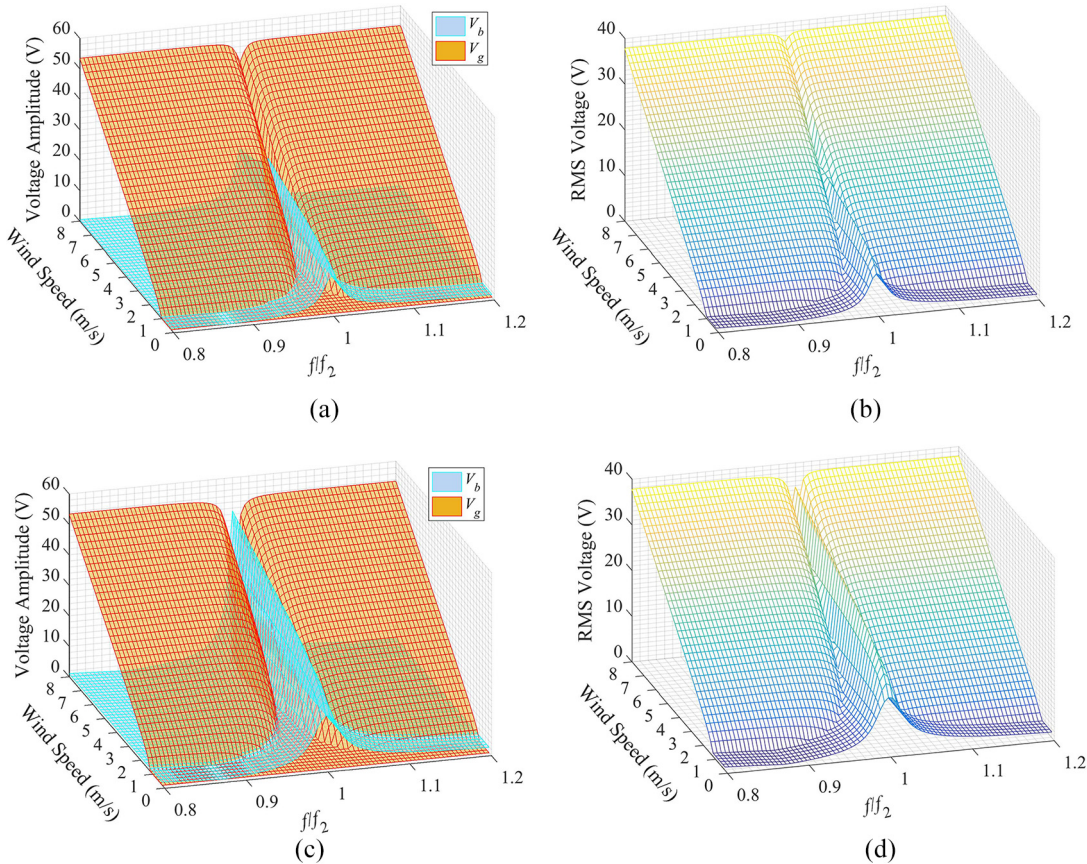


Figure 5. Analytically obtained voltage amplitudes of V_b and V_g versus wind speed U and the non-dimensionless frequency f/f_2 : (a) $A_{cc} = 1 \text{ m/s}^2$ and (c) $A_{cc} = 2 \text{ m/s}^2$; RMS voltage versus wind speed U and the non-dimensionless frequency f/f_2 : (b) $A_{cc} = 1 \text{ m/s}^2$ and (d) $A_{cc} = 2 \text{ m/s}^2$.

of V_b and V_g and the RMS voltage, respectively. As compared to the results under the lower base excitation (i.e. Figure 5(a)), it is observed in Figure 5(c) that the increase of the base excitation does not have a significant effect on V_g , that is, the galloping behavior of the 2DOF PEH. The quenching phenomenon becomes a bit more evident with the increase of the base excitation, the voltage amplitude is only slightly reduced, and the cut-in wind speed slightly increases. Contrarily but unsurprisingly, the increase of the base excitation magnifies V_b , that is, the forced vibration of the 2DOF PEH. Due to the enhancement of the forced vibration by the base excitation, the overall energy harvesting performance (as revealed in Figure 5(c)) around the second resonant frequency is improved. However, from the evolution trend, it can be inferred that the peak-to-valley transition phenomenon is only postponed. By further increasing the wind speed, the peak would eventually transform into a valley. Therefore, under the high wind speed, it can be deduced that the small neighboring region of the second resonance would still be undesired for energy harvesting.

From the above analysis, we can see that Figures 3 and 5 have revealed the global evolution trend of the

energy harvesting performance of the 2DOF PEH around its fundamental and second resonant frequencies. In the following study, to give more in-depth insights into the dynamic behavior of the system, several more detailed case examples under specific wind speeds are presented. In addition, numerical results from circuit simulations are also provided to validate the analytical results.

5.1. Under low wind speed

Under the wind speed of 2 m/s and the base excitation at constant acceleration of 1 m/s², Figure 6(a) shows the analytically calculated voltage amplitudes of different response components with different frequencies around the fundamental resonance of the 2DOF PEH. It can be found that around the fundamental resonance, $V_b \neq 0$ while $V_g \equiv 0$, which indicates that the galloping-induced vibration fails to be incurred and the oscillation motion is dominated by the forced vibration under the base excitation. Figure 6(b) compares the RMS voltages predicted by the analytical and the equivalent circuit models. It is noted that both results match well with each other. In addition to the

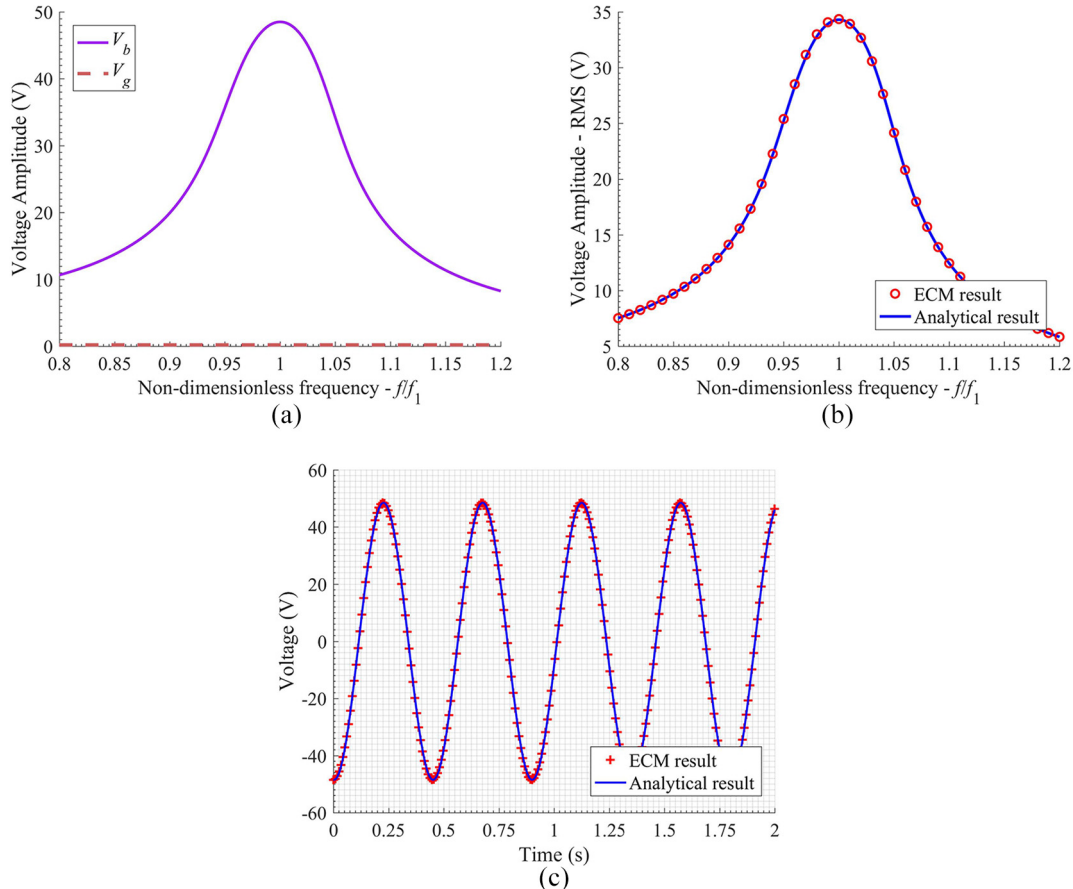


Figure 6. (a) Analytically obtained voltage amplitudes of different harmonic components with different frequencies around the fundamental resonance of the 2DOF PEH under the wind speed of 2 m/s, (b) comparison of the RMS voltages predicted by the analytical and the equivalent circuit models, and (c) comparison of the steady-state responses at the frequency of $f/f_1 = 1$.

frequency response, Figure 6(c) also presents the time-domain (steady-state) responses at the frequency of $f/f_1 = 1$ predicted by both models. A good agreement between both results further validates the analytical solution derived in section 3.

Figure 7(a) shows the analytically calculated voltage amplitudes of different response components with different frequencies around the second resonance of the 2DOF PEH. Different from the behavior around the fundamental resonance, it can be seen that V_g does not constantly equal zero. When the excitation frequency deviates from the second resonant frequency of the 2DOF PEH, V_g becomes non-zero, which implies the activation of the galloping-induced vibration. According to the relationship between the magnitudes of V_b and V_g , Figure 7(a) can be divided into two regions. One region corresponds to the quenching phenomenon, which is just nearby the second resonance frequency of the 2DOF PEH where the system is at resonance from the point of view of forced vibration dynamics. In this region, the forced vibration under the base excitation plays the dominant role, that is, $V_b > V_g$. The rest frequency range represents the other

region where the system is at off-resonance from the point of view of forced vibration dynamics. In this region, the galloping-induced vibration becomes dominant, that is, $V_g > V_b$. Due to this phenomenon, the output voltage from the 2DOF PEH at off-resonance could even become larger than at the frequencies near but away from the exact resonance. The output voltage level at off-resonance is lifted by the galloping-induced vibration phenomenon and becomes almost constant over the frequency range.

To verify the analytical result in Figure 7(a), one can perform a series of transient circuit simulations at different frequencies, then extract the spectral information of the steady-state responses using the Fast Fourier Transform (FFT) approach. In this process, the spectral leakage problem should be avoided to ensure an accurate comparison. As an alternative and more appropriate means, the RMS voltages from both analytical and circuit models are computed and compared for verification. The comparison result is presented in Figure 7(b). The discrete circle points that denote a series of circuit simulation results closely stick to the solid line that represents the analytical result.

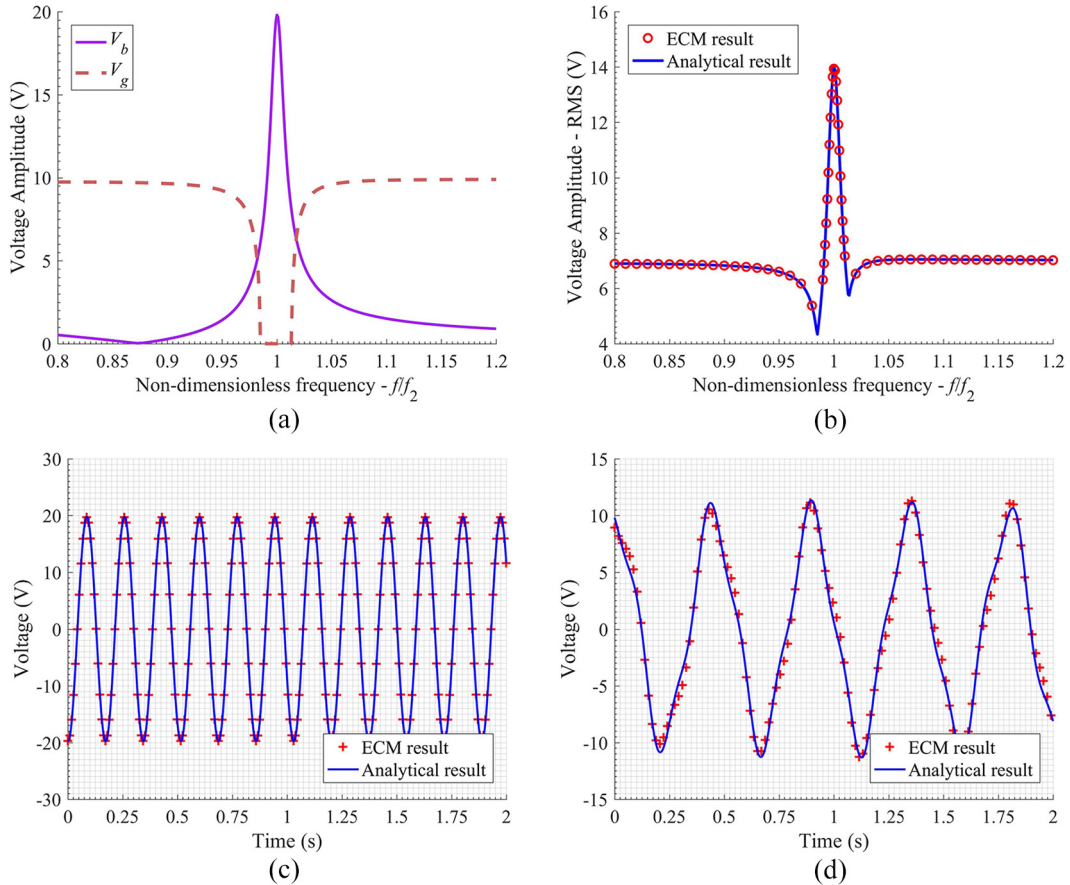


Figure 7. (a) Analytically obtained voltage amplitudes of different harmonic components with different frequencies around the second resonance of the 2DOF PEH under the wind speed of 2 m/s, (b) comparison of the RMS voltages predicted by the analytical and the equivalent circuit models, (c) comparison of the steady-state responses at the frequency of $f/f_2 = 1$, and (d) comparison of the steady-state responses at the frequency of $f/f_2 = 1.1$.

Furthermore, the steady-state time-domain responses predicted by both models at two different frequencies from the aforementioned two different regions are compared in Figure 7(c) and (d). The analytical result overlaps with the circuit simulation result very well. It is observed from Figure 7(c) that the response is a single-frequency harmonic signal, as the excitation frequency is $f/f_2 = 1$ that falls into the region where $V_b > V_g$ and $V_g = 0$. When the excitation frequency is tuned to $f/f_2 = 1.1$ that falls into the region where V_b and V_g co-exist and $V_g > V_b$, the response revealed in Figure 7(d) becomes a quasi-periodic signal that contains two harmonic components. Moreover, one can note that the signal in the same period in Figure 7(d) is more sparse than that in Figure 7(c). This is because the galloping-induced vibration plays the dominant role in Figure 7(d) and the dominant frequency is thus ω_g , which equals to $\omega_1 < \omega_b = \omega_2$.

5.2. Under high wind speed

Subsequently, the wind speed is increased to 6 m/s, while the base acceleration is kept at 1 m/s². Figure

8(a) shows the frequency responses of the magnitudes of V_b and V_g predicted by the analytical solution around the fundamental resonance of the 2DOF PEH. Similar to the behavior in Figure 7(a), the frequency range can be divided into two regions. The 2DOF PEH in the quenching region is under the dominance of the forced vibration driven by the base excitation, that is, $V_b > V_g$. In the other region, the 2DOF PEH is under the dominance of the galloping-induced vibration, that is, $V_g > V_b$. For the same reason of convenience, we compare the RMS voltages from both the analytical calculation and circuit simulation for numerical verification. Figure 8(b) presents the corresponding comparison result. The analytical predictions agree well with the circuit simulation results.

The time-domain voltage responses of the 2DOF PEH at two different frequencies under the steady-state condition are plotted in Figure 8(c) and (d). The response revealed in Figure 8(c) corresponds to a single-frequency oscillation signal, since the excitation frequency is tuned to $f/f_2 = 1$ and only the forced vibration is activated by the base excitation. When f/f_2 is tuned to 1.1, the response becomes a dual-frequency

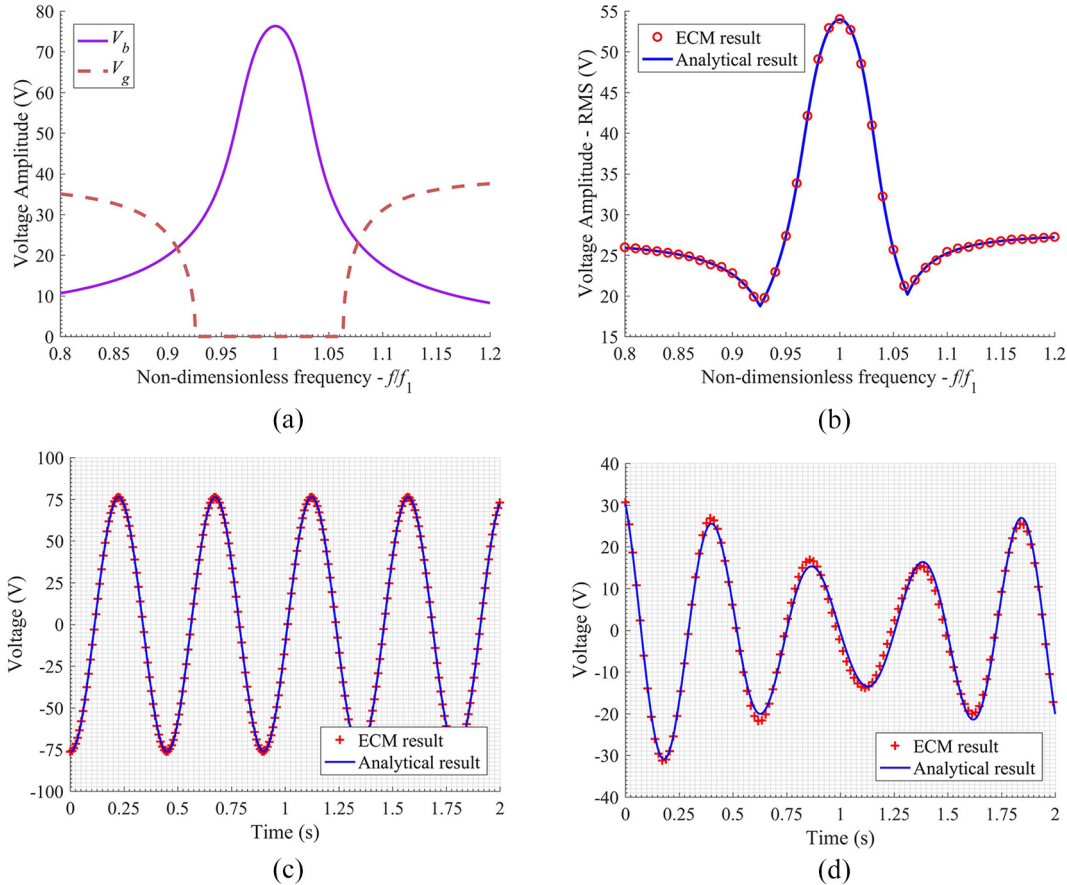


Figure 8. (a) Analytically obtained voltage amplitudes of different harmonic components with different frequencies around the fundamental resonance of the 2DOF PEH under the wind speed of 6 m/s, (b) comparison of the RMS voltages predicted by the analytical and the equivalent circuit models, (c) comparison of the steady-state responses at the frequency of $f/f_1 = 1$, and (d) comparison of the steady-state responses at the frequency of $f/f_1 = 1.1$.

oscillation signal as revealed in Figure 8(d). The explanation for this phenomenon can be found from the analytical result in Figure 8(a): the galloping-induced vibration is incurred and becomes more intense than that of the forced vibration excited by the base displacement. It is worth mentioning that both the single-frequency periodic oscillation and dual-frequency quasi-periodic oscillation have been experimentally observed and reported in Zhao (2020) and Zhao and Yang (2018) for an SDOF PEH under concurrent wind and base excitation.

Under the same wind speed of 6 m/s, the voltage frequency response of the 2DOF PEH around its second resonant frequency is then investigated, and the analytical results are demonstrated in Figure 9(a). Interestingly, it is found that different from previous cases, V_g never becomes zero. Moreover, the magnitude of V_g is almost always larger than that of V_b , which indicates that the galloping-induced vibration would take the dominant role over the entire frequency range around the second resonance of the 2DOF PEH. The analytical RMS voltage is then compared with and

verified by that obtained from circuit simulation in Figure 9(b). It is worth noting that in Figure 9(b), we notice that there abnormally appears a valley rather than a peak at the second resonance of the 2DOF PEH, which means the voltage output at the second resonance of the 2DOF PEH becomes the minimum. The possible explanation behind this phenomenon is that near the second 2DOF PEH, the forced vibration under the base excitation activates the second mode of the 2DOF PEH, while the galloping-induced vibration is the first mode limited cycle oscillation. The out-of-phase motion of the second mode vibration is in contradiction with the in-phase motion of the first mode vibration. Therefore, the co-existence of both vibration modes deteriorates the energy harvesting performance. As a digression of the energy harvesting topic, this phenomenon may have the potential to be employed for the application in vibration suppression since the resonance state is transformed to a state like anti-resonance from the frequency response pattern. Returning from the digression to the result in Figure 9(b), except from the second resonance point, the frequency response is

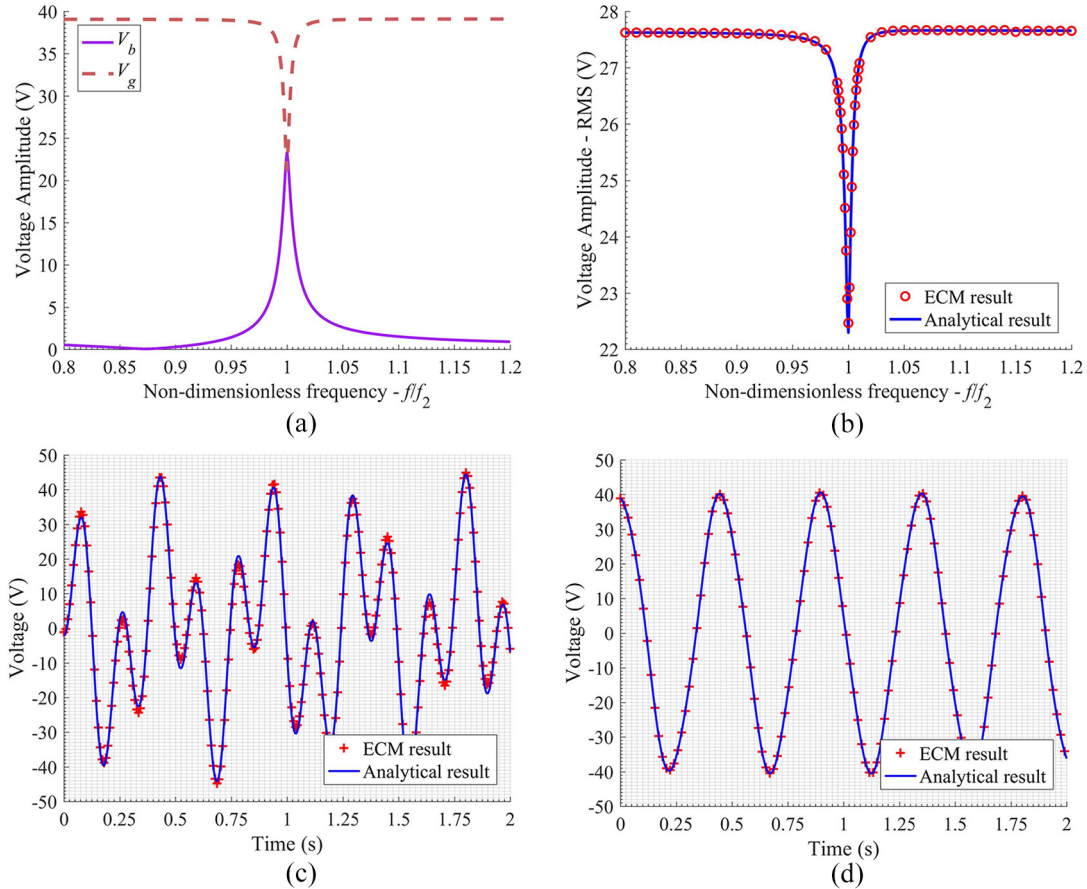


Figure 9. (a) Analytically obtained voltage amplitudes of different harmonic components with different frequencies around the second resonance of the 2DOF PEH under the wind speed of 6 m/s, (b) comparison of the RMS voltages predicted by the analytical and the equivalent circuit models, (c) comparison of the steady-state responses at the frequency of $f/f_2 = 1$, and (d) comparison of the steady-state responses at the frequency of $f/f_2 = 1.1$.

nearly flat, and the magnitude of the RMS voltage over the frequency range is almost constant because the galloping-induced vibration is nearly unaffected by the external base excitation. Finally, the steady-state time-domain responses of the 2DOF PEH at two different frequencies are predicted by the analytical model and compared with the simulation results in Figure 9(c) and (d). Different from previous cases, the response in Figure 9(c) at the frequency of $f/f_2 = 1$ becomes a dual-frequency signal. While the response in Figure 9(d) at the frequency of $f/f_2 = 1.1$ contrarily becomes a quasi-single-frequency signal. The prefix “quasi” is used for being rigorous since it does not truly contain only a single harmonic component, but just because the other component is minor and unnoticeable. These extraordinary phenomena can be well explained by the analytical results in Figure 9(a) for this specific case.

6. Conclusions

In conclusion, this paper has presented a comprehensive theoretical analysis of a 2DOF PEH under

concurrent aeroelastic and base excitation. Using the harmonic balance method, the analytical solution to the 2DOF PEH has been derived by taking account of the combined excitation. An equivalent circuit model of the 2DOF PEH has been established, and the simulation results have verified the analytical solution. Under the same excitation condition, compared to a conventional SDOF PEH, the proposed 2DOF PEH has the following advantages.

- The proposed 2DOF PEH has been found to have a better energy harvesting performance and produce a larger voltage output around the resonance state.
- Besides, owing to the two degrees of freedom, the 2DOF PEH exhibits two resonant peaks that could cover a wide range of spectrum for energy harvesting.

The energy harvesting performance of the 2DOF PEH under the wind flow of low speed (2 m/s) and high speed (6 m/s) has been investigated.

- Near the resonant frequencies, the quenching phenomenon takes place, the galloping-induced vibration is suppressed to zero, and the base excitation plays the dominant role to produce the voltage output.
- Depending on the wind speed and the excitation frequency, the 2DOF PEH may undergo single-frequency harmonic oscillation or dual-frequency quasi-periodic oscillation.
- The quasi-periodic oscillation of the 2DOF PEH, which was experimentally observed in the work of existing literature, has been successfully explained by the analytical solution.
- Besides that, under the high wind speed, near the second resonance of the 2DOF PEH, an interesting peak-to-valley transition phenomenon in the frequency response has been found for the first time. This might be attributed to that the co-existence of the first and second vibration modes stimulated by different excitations deteriorates the energy harvesting performance.

In general, the work presented in this study has paved the way for theoretical analysis of such kind of energy harvesters under concurrent aeroelastic and base excitation. The methodology developed in this paper can be easily applied to other types of SDOF or MDOF galloping-based energy harvesters.

Declaration of conflicting interests

The author(s) declared no potential conflicts of interest with respect to the research, authorship, and/or publication of this article.

Funding

The author(s) disclosed receipt of the following financial support for the research, authorship, and/or publication of this article: The author would like to acknowledge the financial support from China Postdoctoral Science Foundation Funded Project (Grant No. 2020M681577), National Natural Science Foundation of China (Grant No. 12002152), Natural Science Foundation of Jiangsu Province (Grant No. BK20190379), and a project funded by the Priority Academic Program Development of Jiangsu Higher Education Institutions.

ORCID iDs

Junrui Liang  <https://orcid.org/0000-0003-2685-5587>
 Lihua Tang  <https://orcid.org/0000-0001-9031-4190>
 Liya Zhao  <https://orcid.org/0000-0002-6229-4871>

References

- Abdelmoula H and Abdelkefi A (2017) Investigations on the presence of electrical frequency on the characteristics of energy harvesters under base and galloping excitations. *Nonlinear Dynamics* 89(4): 2461–2479.
- Ali M, Arafa M and Elaraby M (2013) Harvesting energy from galloping oscillations. In: *Proceedings of the world congress on engineering*, London, 3–5 July 2013.
- Barrero-Gil A, Alonso G and Sanz-Andres A (2010) Energy harvesting from transverse galloping. *Journal of Sound and Vibration* 329(14): 2873–2883.
- Barrero-Gil A, Vicente-Ludlam D, Gutierrez D, et al. (2020) Enhance of energy harvesting from transverse galloping by actively rotating the galloping body. *Energies* 13(1): 91.
- Bibo A, Abdelkefi A and Daqaq MF (2015a) Modeling and characterization of a piezoelectric energy harvester under combined aerodynamic and base excitations. *Journal of Vibration and Acoustics* 137(3): 031017.
- Bibo A, Alhadidi AH and Daqaq MF (2015b) Exploiting a nonlinear restoring force to improve the performance of flow energy harvesters. *Journal of Applied Physics* 117(4): 045103.
- Bibo A and Daqaq MF (2013a) Investigation of concurrent energy harvesting from ambient vibrations and wind using a single piezoelectric generator. *Applied Physics Letters* 102(24): 243904.
- Bibo A and Daqaq MF (2013b) Energy harvesting under combined aerodynamic and base excitations. *Journal of Sound and Vibration* 332(20): 5086–5102.
- Dai HL, Abdelkefi A and Wang L (2014) Piezoelectric energy harvesting from concurrent vortex-induced vibrations and base excitations. *Nonlinear Dynamics* 77(3): 967–981.
- Eugeni M, Elahi H, Fune F, et al. (2020) Numerical and experimental investigation of piezoelectric energy harvester based on flag-flutter. *Aerospace Science and Technology* 97: 105634.
- Ewere F, Wang G and Cain B (2014) Experimental investigation of galloping piezoelectric energy harvesters with square bluff bodies. *Smart Materials and Structures* 23(10): 104012.
- Fang S, Wang S, Zhou S, et al. (2020) Exploiting the advantages of the centrifugal softening effect in rotational impact energy harvesting. *Applied Physics Letters* 116(6): 063903.
- Hu G, Liang J, Tang L, et al. (2022) Improved theoretical analysis and design guidelines of a two-degree-of-freedom galloping piezoelectric energy harvester. *Journal of Intelligent Material Systems and Structures* 33: 210–230.
- Hu G, Wang J, Qiao H, et al. (2021a) An experimental study of a two-degree-of-freedom galloping energy harvester. *International Journal of Energy Research* 45(2): 3365–3374.
- Hu G, Wang J and Tang L (2021b) A comb-like beam based piezoelectric system for galloping energy harvesting. *Mechanical Systems and Signal Processing* 150: 107301.
- Javed U and Abdelkefi A (2017) Impacts of the aerodynamic force representation on the stability and performance of a galloping-based energy harvester. *Journal of Sound and Vibration* 400: 213–226.
- Lan C, Tang L, Hu G, et al. (2019) Dynamics and performance of a two degree-of-freedom galloping-based piezoelectric energy harvester. *Smart Materials and Structures* 28(4): 045018.
- Li Z, Liu Y, Yin P, et al. (2021) Constituting abrupt magnetic flux density change for power density improvement in electromagnetic energy harvesting. *International Journal of Mechanical Sciences* 198: 106363.
- Liang J and Liao W-H (2012) Improved design and analysis of self-powered synchronized switch interface circuit for

- piezoelectric energy harvesting systems. *IEEE Transactions on Industrial Electronics* 59(4): 1950–1960.
- Liu F-R, Zhang W-M, Peng Z-K, et al. (2019a) Fork-shaped bluff body for enhancing the performance of galloping-based wind energy harvester. *Energy* 183: 92–105.
- Liu F-R, Zhang W-M, Zhao L-C, et al. (2020) Performance enhancement of wind energy harvester utilizing wake flow induced by double upstream flat-plates. *Applied Energy* 257: 114034.
- Liu W, Yuan Z, Zhang S, et al. (2019b) Enhanced broadband generator of dual buckled beams with simultaneous translational and torsional coupling. *Applied Energy* 251: 113412.
- Paulo J and Gaspar P (2010) Review and future trend of energy harvesting methods for portable medical devices. In: *Proceedings of the world congress on engineering*, London, 30 June–2 July 2010.
- Priya S and Inman DJ (2009) *Energy Harvesting Technologies*, vol. 21. New York, NY: Springer.
- Roundy S, Wright PK and Rabaey J (2003) A study of low-level vibrations as a power source for wireless sensor nodes. *Computer Communications* 26(11): 1131–1144.
- Sirohi J and Mahadik R (2011) Piezoelectric wind energy harvester for low-power sensors. *Journal of Intelligent Material Systems and Structures* 22(18): 2215–2228.
- Sirohi J and Mahadik R (2012) Harvesting wind energy using a galloping piezoelectric beam. *Journal of Vibration and Acoustics* 134(1): 011009.
- Staggs J, Ferlemann D and Shenoi S (2017) Wind farm security: Attack surface, targets, scenarios and mitigation. *International Journal of Critical Infrastructure Protection* 17: 3–14.
- Tan T, Hu X, Yan Z, et al. (2019) Enhanced low-velocity wind energy harvesting from transverse galloping with super capacitor. *Energy* 187: 115915.
- Tang L and Yang Y (2012) A multiple-degree-of-freedom piezoelectric energy harvesting model. *Journal of Intelligent Material Systems and Structures* 23(14): 1631–1647.
- Tang L, Zhao L, Yang Y, et al. (2015) Equivalent circuit representation and analysis of galloping-based wind energy harvesting. *IEEE/ASME Transactions on Mechatronics* 20(2): 834–844.
- Wang J, Geng L, Ding L, et al. (2020a) The state-of-the-art review on energy harvesting from flow-induced vibrations. *Applied Energy* 267: 114902.
- Wang J, Geng L, Zhou S, et al. (2020b) Design, modeling and experiments of broadband tristable galloping piezoelectric energy harvester. *Acta Mechanica Sinica* 36: 592–605.
- Wang J, Hu G, Su Z, et al. (2019a) A cross-coupled dual-beam for multi-directional energy harvesting from vortex induced vibrations. *Smart Materials and Structures* 28(12): 12LT02.
- Wang J, Tang L, Zhao L, et al. (2020c) Equivalent circuit representation of a vortex-induced vibration-based energy harvester using a semi-empirical lumped parameter approach. *International Journal of Energy Research* 44(6): 4516–4528.
- Wang J, Zhou S, Zhang Z, et al. (2019b) High-performance piezoelectric wind energy harvester with Y-shaped attachments. *Energy Conversion and Management* 181: 645–652.
- Wu Y, Qiu J, Kojima F, et al. (2019) Design methodology of a frequency up-converting energy harvester based on dual-cantilever and pendulum structures. *AIP Advances* 9(4): 045312.
- Yan Z, Abdelkefi A and Hajj MR (2014) Piezoelectric energy harvesting from hybrid vibrations. *Smart Materials and Structures* 23(2): 025026.
- Yan Z, Lei H, Tan T, et al. (2018) Nonlinear analysis for dual-frequency concurrent energy harvesting. *Mechanical Systems and Signal Processing* 104: 514–535.
- Yan Z, Wang L, Hajj MR, et al. (2020) Energy harvesting from iced-conductor inspired wake galloping. *Extreme Mechanics Letters* 35: 100633.
- Yang Y, Zhao L and Tang L (2013) Comparative study of tip cross-sections for efficient galloping energy harvesting. *Applied Physics Letters* 102(6): 064105.
- Zeadally S, Shaikh FK, Talpur A, et al. (2020) Design architectures for energy harvesting in the Internet of Things. *Renewable and Sustainable Energy Reviews* 128: 109901.
- Zhang M, Hu G and Wang J (2020) Bluff body with built-in piezoelectric cantilever for flow-induced energy harvesting. *International Journal of Energy Research* 44(5): 3762–3777.
- Zhao L (2019) Analytical solutions for a broadband concurrent aeroelastic and base vibratory energy harvester. In: *Active and passive smart structures and integrated systems XII*, Denver, CO, 21 March 2019.
- Zhao L (2020) Synchronization extension using a bistable galloping oscillator for enhanced power generation from concurrent wind and base vibration. *Applied Physics Letters* 116(5): 053904.
- Zhao L, Tang L and Yang Y (2014) Enhanced piezoelectric galloping energy harvesting using 2 degree-of-freedom cut-out cantilever with magnetic interaction. *Japanese Journal of Applied Physics* 53(6): 060302.
- Zhao L and Yang Y (2018) An impact-based broadband aeroelastic energy harvester for concurrent wind and base vibration energy harvesting. *Applied Energy* 212: 233–243.

Appendix

$$P_1 = \frac{(-k_1 m_2 + c_1(c_1 + c_2))\omega_b^2 + C_{e1}c_1\omega_b + k_1(k_1 + k_2 + K_{e1})}{\left\{ \begin{array}{l} m_2^2\omega_b^4 + (-2K_{e1}m_2 + c_1^2 + 2c_1c_2 + c_2^2 - 2k_1m_2 - 2k_2m_2)\omega_b^2 \\ + 2C_{e1}(c_1 + c_2)\omega_b + k_1^2 + (2k_2 + 2K_{e1})k_1 + k_2^2 + 2K_{e1}k_2 + C_{e1}^2 + K_{e1}^2 \end{array} \right\}}$$

$$Q_1 = \frac{c_1 m_2 \omega_b^3 + ((-k_2 - K_{e1})c_1 + c_2 k_1)\omega_b + C_{e1}k_1}{\left\{ \begin{array}{l} m_2^2\omega_b^4 + (-2K_{e1}m_2 + c_1^2 + 2c_1c_2 + c_2^2 - 2k_1m_2 - 2k_2m_2)\omega_b^2 \\ + 2C_{e1}(c_1 + c_2)\omega_b + k_1^2 + (2k_2 + 2K_{e1})k_1 + k_2^2 + 2K_{e1}k_2 + C_{e1}^2 + K_{e1}^2 \end{array} \right\}}$$

$$\begin{aligned}
O_1 &= \frac{Z_b \left(\begin{array}{l} (-K_{e1}m_2 - k_2 m_2 + c_2(c_1 + c_2))\omega_b^2 + C_{e1}(c_1 + 2c_2)\omega_b \\ + K_{e1}^2 + (k_1 + 2k_2)K_{e1} + k_1 k_2 + k_2^2 + C_{e1}^2 \end{array} \right)}{\left\{ \begin{array}{l} m_2^2 \omega_b^4 + (-2K_{e1}m_2 + c_1^2 + 2c_1 c_2 + c_2^2 - 2k_1 m_2 - 2k_2 m_2)\omega_b^2 \\ + 2C_{e1}(c_1 + c_2)\omega_b + K_{e1}^2 + (2k_1 + 2k_2)K_{e1} + k_1^2 + 2k_1 k_2 + k_2^2 + C_{e1}^2 \end{array} \right\}} \\
O_2 &= \frac{(c_2 m_2 \omega_b^3 + m_2 C_{e1} \omega_b^2 + ((k_2 + K_{e1})c_1 - c_2 k_1)\omega_b - C_{e1} k_1)Z_b}{\left\{ \begin{array}{l} m_2^2 \omega_b^4 + (-2k_1 m_2 + (-2k_2 - 2K_{e1})m_2 + (c_1 + c_2)^2)\omega_b^2 \\ + 2C_{e1}(c_1 + c_2)\omega_b + k_1^2 + (2k_2 + 2K_{e1})k_1 + C_{e1}^2 + (k_2 + K_{e1})^2 \end{array} \right\}} \\
\Gamma_1 &= \frac{(-k_1 m_2 + c_1(c_1 + c_2))\omega_g^2 + C_{e2} c_1 \omega_g + k_1(k_1 + k_2 + K_{e2})}{\left\{ \begin{array}{l} m_2^2 \omega_g^4 + (-2K_{e2}m_2 + c_1^2 + 2c_1 c_2 + c_2^2 - 2k_1 m_2 - 2k_2 m_2)\omega_g^2 \\ + 2C_{e2}(c_1 + c_2)\omega_g + k_1^2 + (2k_2 + 2K_{e2})k_1 + k_2^2 + 2K_{e2}k_2 + C_{e2}^2 + K_{e2}^2 \end{array} \right\}} \\
\Gamma_2 &= \frac{c_1 m_2 \omega_g^3 + ((-k_2 - K_{e2})c_1 + c_2 k_1)\omega_g + C_{e2} k_1}{\left\{ \begin{array}{l} m_2^2 \omega_g^4 + (-2K_{e2}m_2 + c_1^2 + 2c_1 c_2 + c_2^2 - 2k_1 m_2 - 2k_2 m_2)\omega_g^2 \\ + 2C_{e2}(c_1 + c_2)\omega_g + k_1^2 + (2k_2 + 2K_{e2})k_1 + k_2^2 + 2K_{e2}k_2 + C_{e2}^2 + K_{e2}^2 \end{array} \right\}} \\
\Gamma_3 &= \frac{-c_1 m_2 \omega_g^3 + ((k_2 + K_{e2})c_1 - c_2 k_1)\omega_g - C_{e2} k_1}{\left\{ \begin{array}{l} m_2^2 \omega_g^4 + (-2K_{e2}m_2 + c_1^2 + 2c_1 c_2 + c_2^2 - 2k_1 m_2 - 2k_2 m_2)\omega_g^2 \\ + 2C_{e2}(c_1 + c_2)\omega_g + k_1^2 + (2k_2 + 2K_{e2})k_1 + k_2^2 + 2K_{e2}k_2 + C_{e2}^2 + K_{e2}^2 \end{array} \right\}} \\
\Gamma_4 &= \frac{(-k_1 m_2 + c_1(c_1 + c_2))\omega_g^2 + C_{e2} c_1 \omega_g + k_1(k_1 + k_2 + K_{e2})}{\left\{ \begin{array}{l} m_2^2 \omega_g^4 + (-2K_{e2}m_2 + c_1^2 + 2c_1 c_2 + c_2^2 - 2k_1 m_2 - 2k_2 m_2)\omega_g^2 \\ + 2C_{e2}(c_1 + c_2)\omega_g + k_1^2 + (2k_2 + 2K_{e2})k_1 + k_2^2 + 2K_{e2}k_2 + C_{e2}^2 + K_{e2}^2 \end{array} \right\}} \\
&\quad \left\{ \begin{array}{l} g_1 = r_{12} \frac{\left[\frac{-6D_B L_{11}^2 \rho s_3 \omega_b^2 \omega_g - 3D_B L_{12}^2 \rho s_3 \omega_g^3 + 4((LU\rho D_B s_1 + 2c_1(\Gamma_1 - 1))\omega_g - 2k_1 \Gamma_2)U}{8U(m_1 \omega_g^2 + c_1 \Gamma_2 \omega_g + k_1(\Gamma_1 - 1))} \right]}{\sqrt{1 + \left[\frac{-6D_B L_{11}^2 \rho s_3 \omega_b^2 \omega_g - 3D_B L_{12}^2 \rho s_3 \omega_g^3 + 4((LU\rho D_B s_1 + 2c_1(\Gamma_1 - 1))\omega_g - 2k_1 \Gamma_2)U}{8U(m_1 \omega_g^2 + c_1 \Gamma_2 \omega_g + k_1(\Gamma_1 - 1))} \right]^2}} \\ h_1 = r_{12} \frac{1}{\sqrt{1 + \left[\frac{-6D_B L_{11}^2 \rho s_3 \omega_b^2 \omega_g - 3D_B L_{12}^2 \rho s_3 \omega_g^3 + 4((LU\rho D_B s_1 + 2c_1(\Gamma_1 - 1))\omega_g - 2k_1 \Gamma_2)U}{8U(m_1 \omega_g^2 + c_1 \Gamma_2 \omega_g + k_1(\Gamma_1 - 1))} \right]^2}} \end{array} \right. \end{aligned}$$